IEEE Access
Multidisciplinary | Rapid Review | Open Access Journal

Received 4 June 2024, accepted 21 June 2024, date of publication 25 June 2024, date of current version 2 July 2024.

Digital Object Identifier 10.1109/ACCESS.2024.3418968

RESEARCH ARTICLE

Optimizing Recurrent Neural Network-Based pH Prediction System of Halochromic Film for Chronic Wound Monitoring

DAEUK KIM[1], RONNIE S. CONCEPCION, II[1], (Member, IEEE), JOSEPH REY H. STA. AGUEDA[1], AND JOHN MARTIN S. MONDRAGON[2]

[1]Department of Manufacturing Engineering and Management, De La Salle University, Manila 1004, Philippines
[2]Department of Biology, De La Salle University, Manila 1004, Philippines

Corresponding author: Daeuk Kim (daeuk_kim@dlsu.edu.ph)

This work was supported in part by the Biomaterials and Tissue Engineering Laboratory (BiMaTEL) of De La Salle University, and in part by the Department of Science and Technology - Philippine Council for Health Research and Development (DOST-PCHRD) as a part of a Smart Multifunctional and Indigenous Dressings Sterilized Using the Electron Beam as Novel Wound Repair Matrices (SMIDERM) Project.

ABSTRACT Chronic wounds, known for their prolonged healing and the associated financial strain on patients, highlight the growing need for effective monitoring methods. One approach to handling chronic wounds involves monitoring biomarkers, with pH emerging as a promising option. Halochromic sensors, designed to detect color changes in response to pH fluctuations, can be employed for monitoring pH variations in wounds. Previous studies have demonstrated the utility of halochromic-based materials in the field of wound management. Nevertheless, it is worth noting that data derived from such sensors may be prone to misinterpretation, particularly when subjected to human visual processing. Hence, this paper aims to develop a pH prediction system based on the fabricated polymer's extracted values of different color channels. As a feature selection, principal component analysis (PCA) was performed to determine the number of significant features, and neighborhood component analysis (NCA) was conducted to eliminate the unrelated elements. Subsequently, an RNN model was developed and enhanced through the application of three distinct metaheuristic optimization algorithms: chernobyl disaster optimizer (CDO), chaos game optimizer (CGO), and coronavirus herd immunity optimization algorithm (CHIO). Following the simulation and evaluation of each optimized RNN model, the CGO-RNN model exhibited the lowest mean squared error (MSE) value of 0.1583, indicating that the RNN with chaos game optimizer stands out as the most effective model for this particular application.

INDEX TERMS Chernobyl disaster optimizer, chaos game optimization, coronavirus herd immunity optimizer, halochromic film, recurrent neural network, metaheuristic algorithms.

I. INTRODUCTION

Chronic wounds are characterized by an extremely slow healing time. Aside from their effect on the physical body, the financial burden accompanying these wounds is another primary problem patients usually suffer from [1]. In fact, it was reported that patients residing in the United States of America spend around a quarter billion dollars every year for treatment. Even though there have been several attempts to develop more effective treatment methods, there has been no progress for the past 25 years due to their pathological complexity [1], [2]. Thus, effective wound management stands out as a crucial component in addressing chronic wounds.

The primary approach to wound monitoring involves visual assessment, where doctors or wound care specialists examine the wound and evaluate it using tools such as the Bates-Jensen Wound Assessment Chart and the Wagner Grading Scale. Although this has long been a standard method, its accuracy

The associate editor coordinating the review of this manuscript and approving it for publication was Yogendra Kumar Prajapati.

is limited due to potential human errors [3]. Another conventional method is wound biopsies, which relies on quantifying bacteria per gram of tissue. However, the presence of bacteria alone is not an absolute indicator of wound infection, leading to debates among medical researchers. Consequently, healthcare practitioners often resort to relying heavily on physical signs such as pain levels and swelling, which may not be prevalent in diabetic patients [4].

Effectively managing chronic wounds involves monitoring biomarkers, with pH emerging as a promising candidate. Elevated pH readings often indicate wound infection [5], and pH demonstrates a robust correlation with slow healing compared to other chemical biomarkers [6]. These findings underscore the significant potential of pH as a valuable sensor for wounds.

Chromism is an optical phenomenon where the color of a specific material changes due to an external stimulus. Depending on this stimulus, chromism can be classified into various types, such as photochromism, solvatochromism, thermochromism, and halochromism [7]. Halochromism refers to when the color changes depending on the pH level [8]. Recently, chromic sensors have been adapted in numerous areas like wearable devices, drug delivery, and personal security because they respond fast, and anyone can easily observe and assess their indication [7].

Among the various chromic sensors, thermochromism-based materials are more commonly used and applied due to the wide range of real-life applications. In 2018, a novel chemical compound composed of manganese violet was integrated to possess thermochromic behavior. Manganese violet was formed using manganese oxide as the base material. Its property was explored by executing different methods, such as x-ray diffraction and infrared spectroscopy. The experiment revealed that the material under investigation can effectively sense temperatures up to 400 degrees Celsius [9]. Additionally, a different thermochromic sensor was introduced in another study [10]. This sensor, designed as a film using polydimethylsiloxane (PDMS) with fluorescent probes, aimed to detect thermal damage in aircraft composites. Comparative analysis with a conventional C-scan device demonstrated its faster and more efficient detection of such damages.

In contrast to the extensive research conducted on other forms of chromism, the scientific investigation of halochromism has been limited. Nevertheless, halochromism can be highly advantageous in specific food packaging and medicine domains. In the study conducted by the researchers [11], a halochromic film was produced to assess the edibility of fish by determining its freshness. Three distinct films with different materials were manufactured and exhibited significant sensitivity. A separate investigation documented the development of a halochromic sensor using the process of electrospinning a solution containing poly(acrylonitrile-co-vinyl acetate) (PAN) and phenolphthalein, an organic pH indicator. The created nanofiber exhibited a pH detection range of 8 to 13. Additionally, it demonstrated exceptional recyclability since its high sensitivity was maintained over many months [12].

The primary purpose of sensors is to gather precise data. However, with the rapid advancements in artificial intelligence, smart sensors have emerged. These sensors collect data and analyze and predict potential outcomes, expanding their utility for more targeted applications [13]. The main application of these smart sensors is color vision sensors, as the human vision system heavily depends on the presence of light. The authors of [14] proposed a color vision system based on deep learning, specifically utilizing a convolutional neural network (CNN) that integrates a U-Net encoder. This system was designed to identify colors in low-light conditions effectively. Furthermore, a hybrid technique consisting of a convolutional neural network (CNN) and a recurrent neural network (RNN) was introduced in [15]. The CNN component is employed to extract features from the color channels of unprocessed images, while the RNN component is utilized for classification tasks.

Optimization is a crucial step in machine learning (ML) algorithms as it aims to achieve precise analysis and interpretation by utilizing an optimized model. Since the outcome of optimization dictates which ML algorithm to adopt, it has become popular to improve ML algorithms through optimization [16]. Lately, there has been a growing emphasis on metaheuristic algorithms within the optimization field. This is due mainly to their distinctive architecture and origin, enabling them to effectively address intricate issues beyond conventional optimization algorithms' capabilities. Furthermore, it is worth noting that metaheuristic algorithms do not necessitate extensive processing resources [17]. Hence, multiple papers proposed optimizing neural network models with novel metaheuristic bio-inspired algorithms. One study [18] chose three optimization algorithms to optimize the transmitter monitoring system. Based on the presented results, a hybrid algorithm constructed using a shuffled frog leap algorithm (SFPA) optimizer and feed-forward neural network (FFNN) produced the best outcome.

Previous studies have demonstrated the utility of halochromic-based materials in the field of wound management. Nevertheless, it is worth noting that data derived from such sensors may be prone to misinterpretation, particularly when subjected to human visual processing. This is primarily due to the inherent limitations in human perception of color change, which are often underestimated [19]. Hence, it is imperative to develop a more dependable and precise way of analysis. The primary objective of this research is to develop an optimized recurrent neural network-based pH prediction system with the goal of minimizing prediction errors.

This study's primary contributions encompass the following aspects: (1) the fabrication of halochromic film using polyvinyl alcohol (PVA), polyethylene glycol (PEG), bromothymol blue (BTB), and glutaraldehyde; (2) the optimization of the recurrent neural network (RNN) model

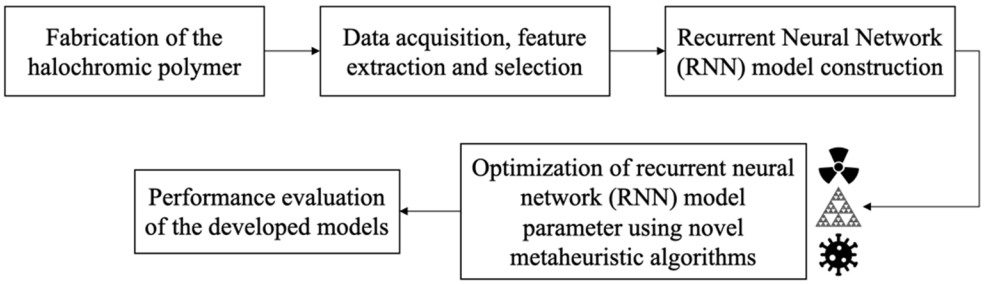

FIGURE 1. Methodological framework.

using the chernobyl disaster optimizer (CDO), the chaos game optimizer (CGO), and the coronavirus herd immunity optimization algorithm (CHIO); and (3) the evaluation and determination of the best performing optimized RNN model. The algorithms mentioned above are procedure-based and have numerous benefits. These entities possess great flexibility and adaptability, rendering them well-suited for intricate real-world optimization issues that present challenges in mathematical modeling. Moreover, explicit mathematical equations are optional for their utilization, making them applicable when mathematical models are unavailable or challenging to develop. They are also highly effective in quickly navigating solution spaces, as they can adjust their methods in response to changing settings [20].

Although CGO and CHIO have been used to tackle practical applications like solar optimization, the potential application of CDO still needs to be explored. However, these algorithms have yet to be utilized in this application and subjected to comparative analysis. Therefore, this work can be a foundational reference for forthcoming research endeavors.

II. MATERIALS AND METHODS

This part of the paper contains five main stages, as shown in Fig. 1. Stage 1 involves the fabrication of the hydrogel film using polyvinyl alcohol (PVA), polyethylene glycol (PEG), bromothymol blue (BTB), and glutaraldehyde. In stage 2, the halochromic behavior of the fabricated films was observed and gathered as data by capturing the images, and image segmentation was performed to extract multiple color features. Principal component analysis (PCA) and neighborhood component analysis (NCA) were executed for feature selection. In stage 3, the newly generated dataset based on feature selection and extraction results was utilized to train the RNN model. Combinations of various numbers of hidden layers were used to predict pH level based on the specific color features, and the outcome was saved as a dataset to create a corresponding fitness function. Stage 4 optimizes the constructed RNN mode using three novel optimization algorithms. Lastly, in stage 5, each optimized model was evaluated to determine the best-performing one.

A. FABRICATION OF THE HALOCHROMIC FILM

To produce a halochromic film, 7.5 grams of PVA (Fujifilm Wako Pure Chemical Corporation, Japan) were added to 75 ml of distilled water heated to a minimum of 70°C. The PVA solution was stirred at 600 rpm using a magnetic stirrer for 30 minutes while maintaining a temperature of 70–90 °C. Subsequently, the heating pad was turned off, and a PEG solution (Xilong Scientific Co., China) with concentrations varying from 6 to 10 wt/vol% was introduced into the mixture. A specific quantity of BTB (Sinopharm Chemical Reagent Co., China) was added as a pH indicator. 3 ml of glutaraldehyde (Sigma-Aldrich Corp., United States of America) for chemical crosslinking was added, and the mixture was stirred for 30 minutes to facilitate the crosslinking process. Table 1 presents the sample codes alongside their respective precise concentrations of polyethylene glycol (PEG) and bromothymol blue (BTB). Each sample solution was poured into a mold, creating 270 distinct hydrogel film specimens. Following this, the samples underwent a desiccation process within a controlled environment, housed within a desiccator, for a duration of one week to ensure thorough drying of the films. The comprehensive fabrication process is visually illustrated in Fig. 2. The dimensional attributes of the desiccated samples are documented in Table 2. At the same time, Fig. 3 offers a detailed representation of both the surface and cross-sectional view of the fabricated films.

TABLE 1. The specific concentration of PEG and BTB in each sample.

Sample Code	PVA (wt/vol%)	PEG (wt/vol%)	BTB (wt/vol%)
P6B01			0.01
P6B03		6	0.03
P6B05			0.05
P8B01			0.01
P8B03	10	8	0.03
P8B05			0.05
P10B01			0.01
P10B03		10	0.03
P10B05			0.05

B. DATA ACQUISITION, FEATURE EXTRACTION AND SELECTION

Prior to capturing images, pH buffer solutions ranging from 6 to 10 were prepared. Phosphate buffer solutions with pH 6 to 8 were created using potassium dihydrogen phosphate (HiMedia Laboratories Pvt. Ltd., India), while borate buffer solutions with pH 9 and 10 were made with sodium tetraborate (Dalkem Corporation, Philippines). Each solution (8 ml) was dispensed into a petri dish and positioned on

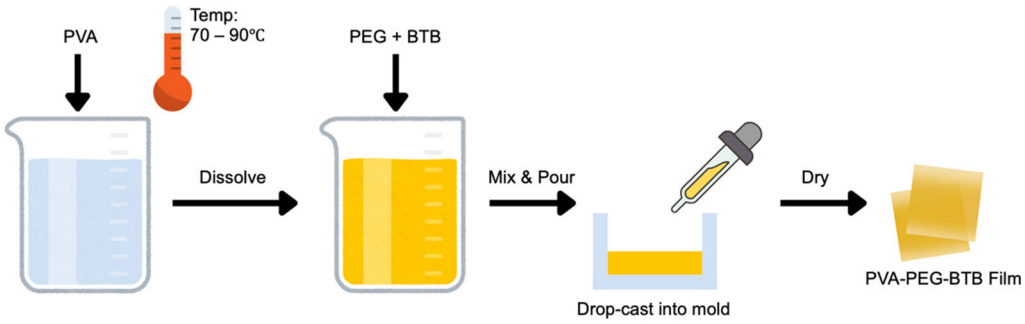

FIGURE 2. Fabrication process of PVA-PEG-BTB halochromic film.

TABLE 2. Dimension of the fabricated film.

Attribute	Unit	Value
Length		1 (±0.1)
Width	mm	1 (±0.1)
Thickness		0.13 (±0.03)

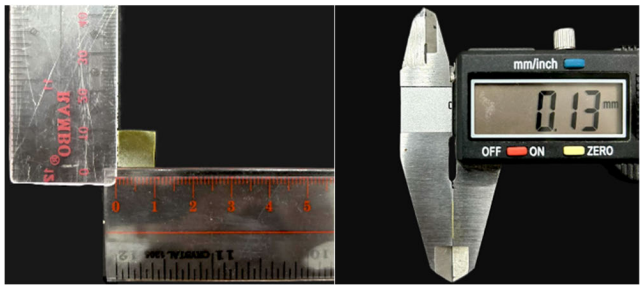

FIGURE 3. Surface and cross-sectional views of the fabricated film.

the 3D printed platform for data collection. A webcam (PK-925H Full HD 1080P Model, A4Tech, Taiwan) connected to a laptop was programmed to record the video and save frame shots, with the program running for 5 minutes to observe the halochromic behavior of the film at different pH levels.

To perform feature extraction, the images were first segmented to remove the background. The final images of each sample were categorized and saved in the designated folder. Using MATLAB R2022b software, every image was converted into CIELAB color space. Among the various available options, the LAB color space was chosen because it is widely accepted as a global standard in detecting color changes in an image, and it was intended to mimic the human vision system. The color thresholder toolbox was utilized to establish the minimum and maximum values for each channel, namely channel L, channel a, and channel b, across all images. A mask was generated in accordance with the specified thresholds. Any component less than 150 pixels was removed to refine the generated mask further. Using this mask, a final segmented image was produced. Fig. 4 shows the step-by-step process of image segmentation performed in this study.

As a next step, the main channels of RGB (red, green, blue), HSV (hue, saturation, value), La∗b∗ (lightness, red-yellow, blue-green), and YCbCr (luminance, chrominance

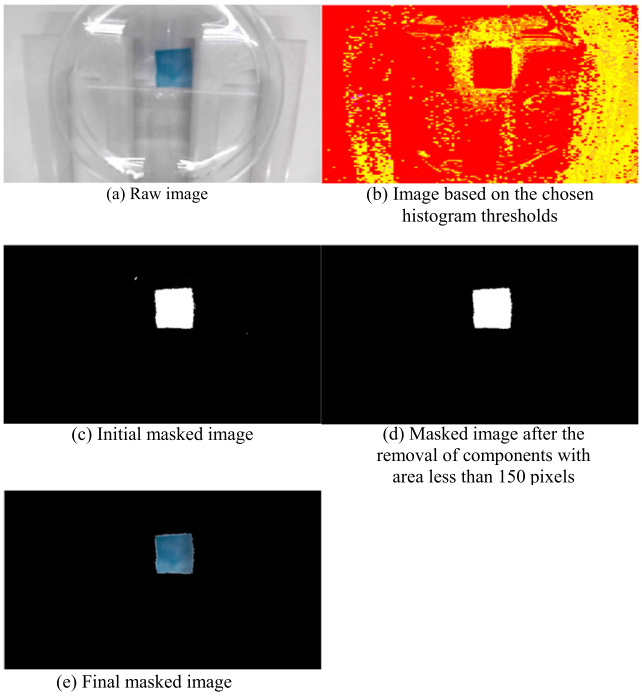

(a) Raw image

(b) Image based on the chosen histogram thresholds

(c) Initial masked image

(d) Masked image after the removal of components with area less than 150 pixels

(e) Final masked image

FIGURE 4. Process of image segmentation through color thresholding.

blue, chrominance red), were extracted and stored as input variables. As a consequence, a total of twelve input features were obtained, necessitating the necessity for feature reduction. Feature selection is a widely recognized strategy in machine learning that improves training performance by focusing solely on relevant features. Therefore, principal component analysis (PCA) was performed to determine the number of significant features, and neighborhood component analysis (NCA) was conducted to eliminate the unrelated elements.

C. CONSTRUCTION OF RECURRENT NEURAL NETWORK (RNN) MODEL AND DATA COLLECTION

From the 270 fabricated films, each film was used to generate 1 data row entry, producing 270 entries as a total. Based on this dataset, a recurrent neural network (RNN) model was constructed and trained. RNN is a type of neural network that can include additional feedback in deciding between

feedback loops. The advantages of RNN are its outstanding performance while requiring low computing capacity and its capability to be applied to establishing attractors between the variables. It also has drawbacks like difficulty determining the optimal hyperparameters for training and weak architecture constancy [21]. The structure of RNN is presented in Fig. 5.

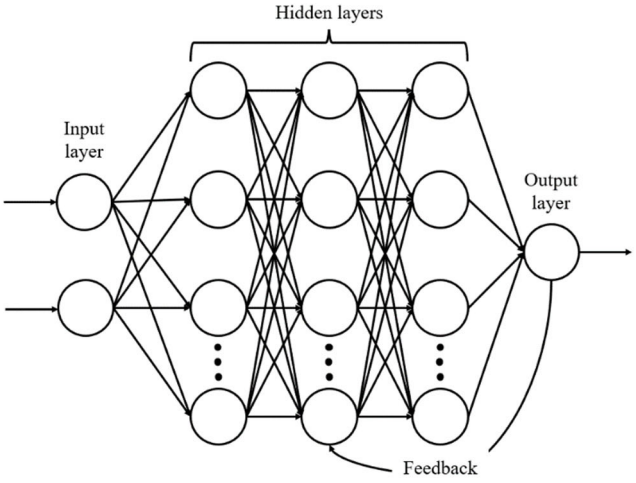

FIGURE 5. Network architecture of RNN.

Different combinations consisting of *logsig*, *tansig*, and *purelin* functions were tested to determine the optimum combination of activation functions for each hidden layer. Incorporating non-linearity is crucial in developing an RNN model since it enables recording intricate patterns within the data. Since the purelin function describes the linear relationship, it is often used as an output layer to present a direct correlation between the input and output variables. Nevertheless, including the purelin function in a hidden layer may be beneficial if a simple network is enough to comprehend the data or address the gradient flow issue. Several studies used these three transfer functions as options in constructing the hidden layers for neural networks [22], [23]. The number of layers for the hidden layers was set as 500, 200, and 100, and each combination was trained for 1,000 epochs. The result of each trial was collected and compared to finalize which set of activation functions to use.

D. OPTIMIZATION OF RNN MODEL USING CHERNOBYL DISASTER OPTIMIZER (CDO), CHAOS GAME OPTIMIZER (CGO), AND CORONAVIRUS HERD IMMUNITY OPTIMIZER (CHIO)

Using the constructed RNN model, a dataset was needed to be gathered to feed Genetic Programming Toolbox for the Identification of Physical Systems version 2 (GPTIPS2), a MATLAB-embedded software that deploys multi-gene symbolic regression genetic programming (MSRGP). GPTIPS2 provides a variety of mathematical models that could be used as fitness functions and visualizations of the model's performance. In determining the number of data points, the design of the experiment (DOE) feature in Minitab statistical software was utilized. Among the available options for DOE, the Taguchi method was selected since it is a statistical tool known to generate robust DOE. In any engineering application, achieving robust design is essential because it is all about producing and maintaining quality without interference from other factors. For the type of design, a mixed-level design with three factors was chosen to generate a total of 36 runs. Level values for the first factor, or number of hidden layer 1, were set as [500, 1000], [200, 400, 600] for the second factor (hidden layer 2), and [100, 300, 500] for the last factor (hidden layer 3). Based on the generated parameters, a dataset containing 36 combination values was collected.

Table 3 presents the hyperparameters assigned to the model within the GPTIPS2 framework. The population was established at 100, while the number of generations was designated as 100. The competition was structured so that 80 individuals were selected to participate, with just 10 percent being chosen for advancement to the subsequent generation. The maximum number of genes and tree depth parameters were configured to be 20 and 10, respectively. A set of 20 training sessions was conducted based on the given parameters, and the resulting fitness functions mean square error (MSE) as output variable and number of hidden layers as input variables were determined.

TABLE 3. Hyperparameters used in implementing GPTIPS2.

Hyperparameter	Value
Population	100
Generations	100
Input variables	3
Training instances	20
Tournament size	80
Elite fraction	0.1
Tournament probability	0.4
Max genes	20
Max tree depth	10

Three different algorithms, chernobyl disaster optimizer (CDO), chaos game optimizer (CGO), and coronavirus herd immunity optimization algorithm (CHIO) were explored for the optimization process. Chernobyl disaster optimizer is a metaheuristic optimization algorithm that was inspired by the explosion of a nuclear power plant in Chernobyl back in 1986. When there is radiation exposure, three kinds of particles, alpha, beta, and gamma, expand across the nearby area. The gradient descent factor of each particle can be computed using the following equations:

$$v_\alpha = 0.25 \cdot (X_\alpha(t) - \rho_\alpha \cdot \Delta_\alpha) \quad (1)$$

$$v_\beta = 0.5 \cdot \left(X_\beta(t) - \rho_\beta \cdot \Delta_\beta\right) \quad (2)$$

$$v_\gamma = \left(X_\gamma(t) - \rho_\gamma \cdot \Delta_\gamma\right) \quad (3)$$

where $v, X, \rho, and \Delta$ are the gradient factor, the current position, the propagation, and the distance between the particle and the subject of exposure of each particle [24].

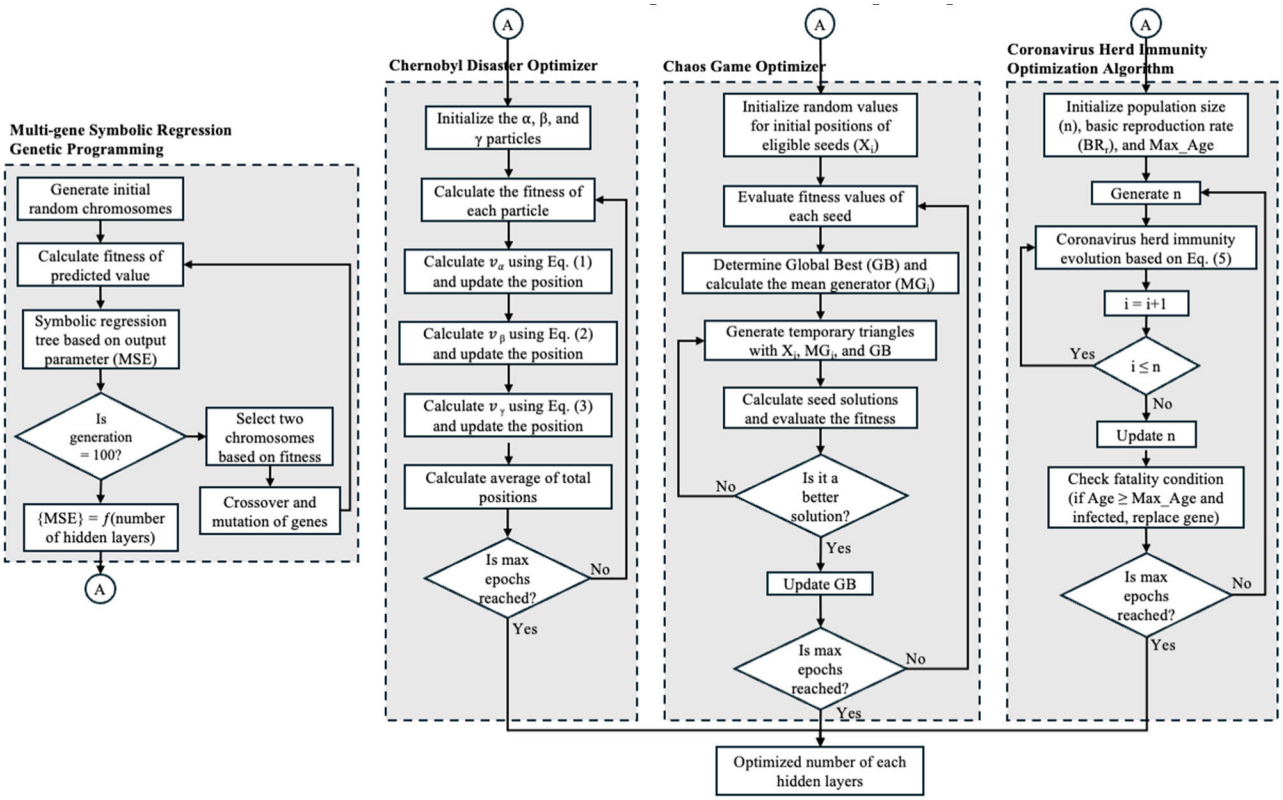

FIGURE 6. Process flowchart of optimization using multi-gene symbolic regression genetic programming, CDO, CGO, and CHIO.

Chaos game optimization algorithm (CGO) is a mathematical-based metaheuristic optimization algorithm that was developed by applying the concept of chaos theory and the mechanism of fractal generation. In simple words, a chaos game is a method of producing fractals by initiating a certain polygon, in this case, a Sierpinski triangle. CGO contemplates various possible solutions (X_i) based on the multiple initial points, also called seeds. Equation (4) shows the mathematical representation of the aforementioned process:

$$X = \begin{bmatrix} X_1 \\ X_2 \\ \vdots \\ X_i \\ \vdots \\ X_n \end{bmatrix} = \begin{bmatrix} x_1^1 & x_1^2 & \cdots & x_1^j & \cdots & x_1^d \\ x_2^1 & x_2^2 & \cdots & x_1^j & \cdots & x_2^d \\ \vdots & \vdots & \vdots & \vdots & \ddots & \vdots \\ x_i^1 & x_i^2 & \cdots & x_i^j & \cdots & x_i^d \\ \vdots & \vdots & \vdots & \vdots & \ddots & \vdots \\ x_n^1 & x_n^2 & \cdots & x_n^j & \cdots & x_n^d \end{bmatrix}, \quad \begin{cases} i = 1, 2, \ldots, n \\ j = 1, 2, \ldots, d \end{cases} \tag{4}$$

where n represents the number of potential solution sets and d describes its dimension [25].

The last adopted optimization algorithm is the coronavirus herd immunity optimization algorithm (CHIO), which was motivated by the concept of herd immunity. During the height of the COVID-19 pandemic, many European nations, including the United Kingdom of Great Britain, pursued a strategy to attain herd immunity. This approach entails a scenario in which a significant portion of the population develops immunity to the virus, reducing its overall transmissibility. One core factor affecting herd immunity is the reproduction rate, denoted by BR_r, which portrays the rate of infection based on the ongoing status. Three rules are used to determine the establishment of herd immunity, which serve as the backbone of this algorithm. Equation (5) represents these rules:

$$x_i^j(t+1) \leftarrow \begin{cases} x_i^j(t), & r \geq BR_r \\ C(x_i^j(t)), & r < \frac{1}{3} \times BR_r \leftarrow \textit{infected case} \\ N(x_i^j(t)), & r < \frac{2}{3} \times BR_r \leftarrow \textit{susceptible case} \\ R(x_i^j(t)), & r < BR_r \leftarrow \textit{immuned case} \end{cases} \tag{5}$$

where x_i^j is the gene in a randomly selected case and r is the range of the rate from 0 to 1 activation functions to use [26].

Fig. 6 illustrates the process flowchart of the optimization performed in this study. The chart details the construction of the fitness function using GPTIPS2 and its optimization using the three specified algorithms. A copy of the codes will be provided to readers upon request.

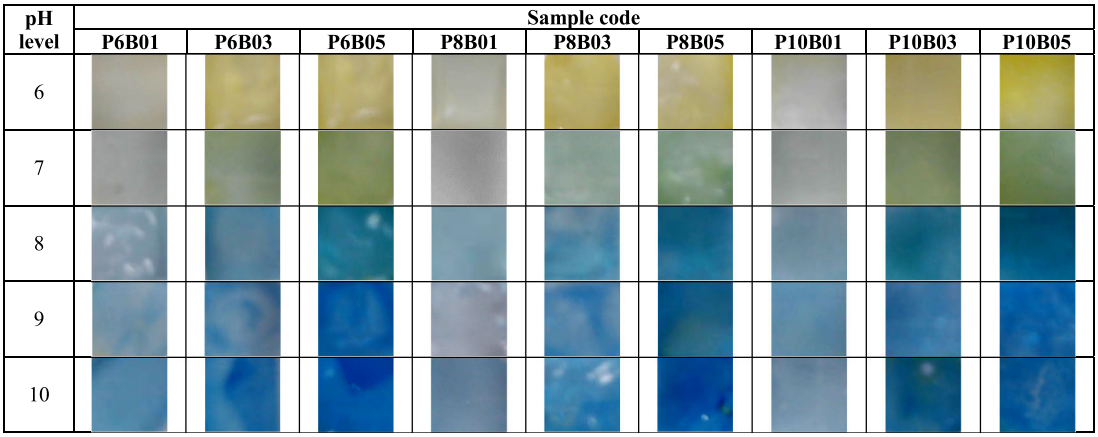

FIGURE 7. Color change of each sample from pH 6 to 10.

E. PERFORMANCE EVALUATION OF THE DEVELOPED RNN MODELS

After determining the optimal parameter values for each hidden layer through a range of optimization algorithms, these values were utilized to train and simulate the RNN model. The evaluation metrics include mean square error (MSE), root mean squared error (RMSE), mean absolute error (MAE), and the coefficient of determination (R^2). The following equations were employed to calculate these metrics:

$$MSE = \frac{1}{n}\sum_{i=1}^{n}(Y_i - \hat{Y}_i)^2 \tag{6}$$

$$RMSE = \sqrt{\frac{1}{n}\sum_{i=1}^{n}(Y_i - \hat{Y}_i)^2} \tag{7}$$

$$MAE = \frac{1}{n}\sum_{i=1}^{n}|Y_i - \hat{Y}_i| \tag{8}$$

$$R^2 = 1 - \frac{\sum_{i=1}^{n}(Y_i - \hat{Y}_i)^2}{\sum_{i=1}^{n}(Y_i - \bar{Y}_i)^2} \tag{9}$$

where n equals the number of data points while Y_i, $\hat{Y}_i$ and $\bar{Y}_i$ are the actual values, predicted values, and the mean of actual values. Furthermore, the Bland-Altman plot analysis was used to visualize the results because it is a straightforward method to assess bias between two measurement methods by examining the mean differences and helps estimate an agreement interval, within which 95% of the differences between the two sets of values [27].

III. RESULTS AND DISCUSSION

Chronic wounds exhibit a pH range of 6.2 to 8.9 [4]. Given this, BTB emerged as the most suitable pH indicator, displaying a color shift from yellow to blue with increasing pH. Fig. 7 illustrates the halochromic response of the developed polymer to varying pH solutions over 5 minutes. The images reveal that all samples remained yellow at pH 6, turned green and blue at pH 7 and 8. With an increase in pH to 9 and 10, there's a noticeable deepening of the blue color intensity. Consequently, this halochromic behavior in the fabricated polymers may serve as an indicator of the transition from a normal wound to a chronic wound.

A. FEATURE SELECTION BASED ON PRINCIPAL COMPONENT ANALYSIS (PCA) AND NEIGHBORHOOD COMPONENT ANALYSIS (NCA)

Principal component analysis (PCA) is a statistical method that can streamline the data while keeping the essential components. During PCA, eigenvalues, particular factors based on a linear combination, get extracted to serve as a basis for comparing each component [28]. The scree plot graph generated by Minitab statistical software is shown in Fig. 8. The original dataset consists of 12 input variables, the average value of red, green, and blue channels under the RGB spectrum, hue, saturation, and value channels under the HSV spectrum; l, a, and b channels under the Lab spectrum; and lastly, luminance, chrominance blue, and chrominance red channels under the YCbCr spectrum; and one output variable, pH level ranging from 6 to 10 with an increment of 1, making a total of 13 components. Conventionally, the eigenvalue must be higher than 1 for a component to be considered significant. Based on the graph below, only two components have an

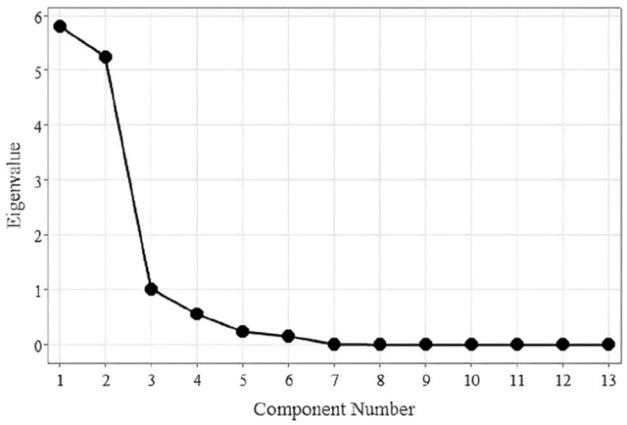

FIGURE 8. Scree plot graph based on principal component analysis (PCA).

eigenvalue above 1, which indicates the number of components or features that need to be selected. However, PCA only provides how many features there are; it does not guarantee which component corresponds to a specific variable. Neighborhood component analysis (NCA) was also implemented to pinpoint these features precisely. As presented in Fig. 9, only two features, the red and blue components of the RGB color spectrum, had feature weights higher than 2.5, while zero for the others. Thus, these two components with matching output values were selected and extracted to produce a new dataset for succeeding procedures.

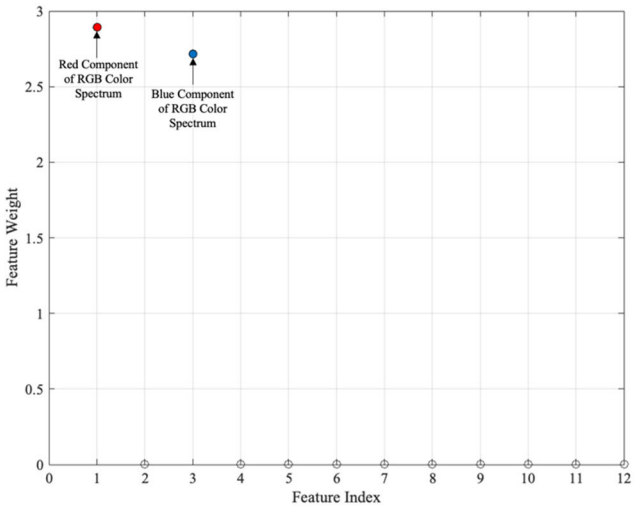

FIGURE 9. Result of neighborhood component analysis (NCA).

B. CONSTRUCTION AND SIMULATION OF CDO-RNN, CGO-RNN, AND CHIO-RNN MODELS

The next step involved determining the best combination of activation functions for each hidden layer based on the updated dataset. Table 4 shows the top three combinations of activation functions, with the top 1 having the smallest MSE value. The combination of purelin, tansig, and logsig functions for the respective hidden layers displayed the lowest MSE value of 1.12×10^{-4}, followed by purelin, logsig, and logsig functions with a value of 1.19×10^{-3}. The set of tansig, logsig, and logsig activation functions ranked third with an MSE value of 1.25×10^{-3}. However, the difference between the second and third combinations was very minimal.

TABLE 4. Best performing combinations of activation functions.

Rank	Activation Functions				Training Functions	MSE
	Hidden layer 1	Hidden layer 2	Hidden layer 3	Output layer		
1	purelin	tansig	logsig	purelin	trainscg	1.12×10^{-4}
2	purelin	logsig	logsig	purelin	trainscg	1.19×10^{-3}
3	tansig	logsig	logsig	purelin	trainscg	1.25×10^{-3}

Following the results of Taguchi DOE and the determined set of activation functions, another dataset was produced, which was utilized to produce the fitness function as represented by Equation (10). It is ideal to reach the r-squared (R^2) value of 1 when creating a fitness function, but the R^2 value of the generated fitness function was only 0.847. One possible explanation could be the lack of a dataset, as GPTIPS2 usually requires massive data to generate a fitness function with a high R^2 value. Since the Taguchi method was adopted as DOE, a robust dataset with only 36 data points was used. Nevertheless, considering the nature of the dataset, the generated fitness function still had an acceptable R^2 value with a low complexity level. This fitness function, in which each variable corresponds to the number of hidden layers, was employed in the three different optimization algorithms, particularly Chernobyl disaster optimizer (CDO), chaos game optimizer (CGO), and coronavirus herd immunity optimizer (CHIO).

$$\begin{aligned} MSE = {} & 7.34e^{-7}x_1 - 6.13e^{-5}x_2 + 6.24e^{-6}x_3 \\ & - 0.0132\sin(x_1x_3) \\ & - 0.0355\sin(x_2) + 4.16e^{-7}x_1x_2 \\ & + 9.63e^{-8}x_1x_3 - 9.0e^{-6}x_1x_2^{\frac{1}{2}} \\ & + 1.51e^{-5}(x_2x_3)^{\frac{1}{2}} - 1.4e^{-7}x_3^2 \\ & - 2.26e^{-7}x_2x_3\sin(x_3) + 0.00549 \end{aligned} \tag{10}$$

Fig. 10 presents the convergence graph of each algorithm applied in this paper. As shown, CGO converged first, followed by CDO, and CHIO at last. To be specific, CGO converged at the 7th iteration and reached its maximum fitness function value at the 571st iteration. For the CDO, it converged at the 92nd iteration, while CHIO converged at the 141st. Even though CDO converged before CHIO, in the end, CHIO generated a lower predicted MSE value, as observed in the zoomed section below. It was seen that once CDO converged, it reached its maximum fitness function value and maintained it until the last iteration, unlike CHIO, which still gradually decreased even after the convergence. CGO displayed the most optimal convergence behavior from these algorithms. Table 5 presents the fitness value of each algorithm, and CGO produced the lowest value.

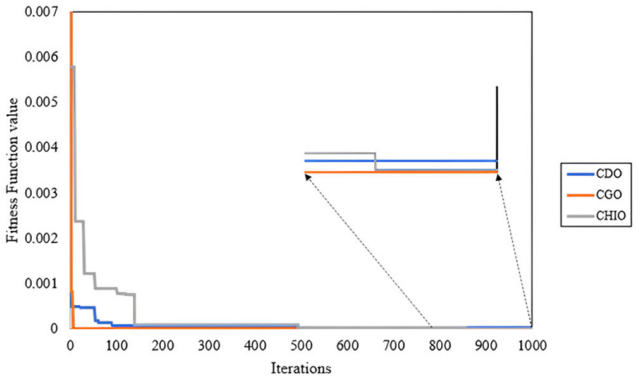

FIGURE 10. Convergence graph of different optimization algorithms.

TABLE 5. Fitness value of each algorithm.

Optimization algorithm	Hidden layer 1	Hidden layer 2	Hidden layer 3	Fitness value
CDO	500	216	114	1.94×10^{-5}
CGO	500	215	166	3.50×10^{-7}
CHIO	596	310	335	3.83×10^{-6}

C. PERFORMANCE EVALUATION OF CDO-RNN, CGO-RNN, and CHIO-RNN MODELS

The performance evaluation of the CDO-RNN, CGO-RNN, and CHIO-RNN models is summarized in Table 6. During training, the CHIO-RNN model demonstrated the best performance, achieving the lowest MSE, RMSE, and MAE values and the highest R^2 value. However, the CGO-RNN model outperformed the others on the testing dataset, with an MSE of 0.1583, an RMSE of 0.3979, an MAE of 0.3021, and an R^2 value of 0.8502. The R^2 value of the CGO-RNN model can be attributed to the fitness function used in its development. The fitness function, derived from multi-gene symbolic regression genetic programming (MSRGP), had an R^2 value of 0.847, as previously mentioned. In addition, based on the predicted fitness value, the CGO-RNN model was expected to perform the best, which was confirmed by these metric values.

Figure 11 shows the Bland-Altman plots for the CDO-RNN, CGO-RNN, and CHIO-RNN models. In these plots, the center line represents the mean difference, indicating the average bias between actual and predicted values. Ideally, this line should be close to zero. The CDO-RNN model produced the most minor mean difference of 1.55×10^{-2} among the three models. Another critical aspect of the Bland-Altman plot is the limits of agreement, indicated by the red dashed lines. A narrower range between these lines signifies better agreement between the actual and predicted values. The CGO-RNN model demonstrated the narrowest range, indicating the best agreement among the three models. Regarding outliers, the CGO-RNN model had the fewest outliers, with most data points falling close to the limits of agreement, further supporting its superior performance in agreement between actual and predicted values.

The increasing need for innovative technology capable of continuously monitoring bio-signals has resulted in the development of wearable sensors. The data acquired from these devices must undergo appropriate processing to optimize the efficacy of wearable sensors. Artificial intelligence (AI) enables efficient processing of vast quantities of data, as AI algorithms can systematically examine the data, extract pertinent information, and generate valuable predictions. The utilization of recurrent neural networks (RNNs) has been observed in the development of these devices due to their ability to provide enhanced discriminative capabilities compared to other machine learning algorithms. This is primarily attributed to the RNN's capacity to encode and learn time-sequential information effectively, and multiple investigations have proven its efficacy [29], [30]. Therefore, this

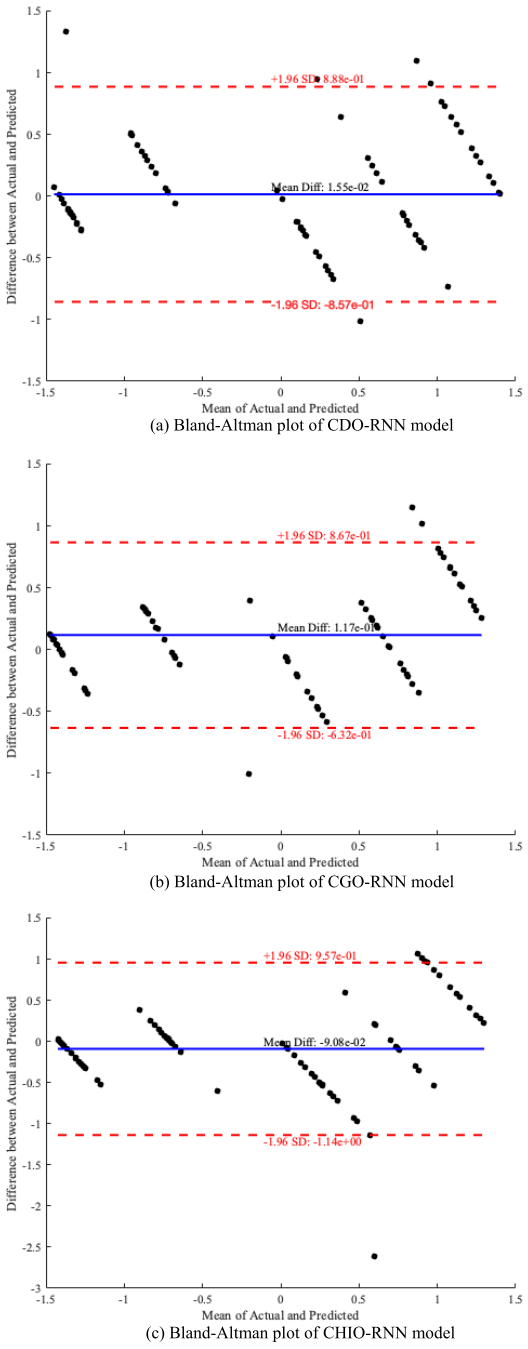

(a) Bland-Altman plot of CDO-RNN model

(b) Bland-Altman plot of CGO-RNN model

(c) Bland-Altman plot of CHIO-RNN model

FIGURE 11. Bland-Altman plot of CDO-RNN, CGO-RNN, and CHIO-RNN models.

study focused on optimizing the Recurrent Neural Network (RNN) to minimize Mean Squared Error (MSE). The resulting MSE of the optimized RNN model was notably low, suggesting its viability for integration into color-vision-based sensor systems designed for halochromic hydrogels. Table 7 provides a comparative analysis of this study and others, aiming to predict pH using various machine-learning algorithms. By examining different metrics, it's evident that this study successfully developed models of acceptable quality.

TABLE 6. Performance Evaluation of CDO-RNN, CGO-RNN, and CHIO-RNN models.

Model	Hidden layer 1	Hidden layer 2	Hidden layer 3	Training				Validation				Testing			
				MSE	RMSE	MAE	R^2	MSE	RMSE	MAE	R^2	MSE	RMSE	MAE	R^2
CDO-RNN	500	216	114	0.1045	0.3233	0.2505	0.8954	0.2840	0.5330	0.3900	0.7015	0.1958	0.4425	0.3443	0.8029
CGO-RNN	500	215	166	0.1708	0.4133	0.3145	0.8316	0.1511	0.3887	0.2877	0.8251	0.1583	0.3979	0.3021	0.8502
CHIO-RNN	596	310	335	0.0869	0.2948	0.2173	0.9106	0.1615	0.4019	0.3221	0.8463	0.2905	0.5390	0.8463	0.6972

TABLE 7. Comparison of other related studies and this work.

Predicting element	Sensor type	Algorithm	Evaluation metrics	Performance score	Reference
pH, dissolved O_2	Fluorescence-based optical chemical sensor	eXtreme Gradient Boosting (XGBoost)	MAE RMSE	0.196 0.4421	[31]
pH	Visible near-infrared (Vis-NIR) spectroscopy	One-dimensional convolutional neural network	RMSE R^2	0.7925 0.8515	[32]
pH	Colorimetric sensor	RNN with chaos game optimizer (CGO)	MSE RMSE MAE R^2	0.1583 0.3979 0.3021 0.8502	This work

IV. CONCLUSION

This study presents a pH prediction system for fabricated halochromic film, utilizing computer vision and artificial intelligence techniques. Based on feature selection results, the red and blue channels of the RGB color spectrum were chosen as input variables. To optimize the Recurrent Neural Network (RNN) model, three metaheuristic optimization algorithms were employed: the chernobyl Disaster Optimizer (CDO), the chaos game optimizer (CGO), and the coronavirus herd immunity optimization algorithm (CHIO). Among these, the CGO-RNN model demonstrated the best performance, achieving the lowest predicted Mean Squared Error (MSE) value of 0.1583. While the proposed model generated acceptable results, further improvements can be made by developing a more accurate fitness function, increasing the size of the dataset, and enhancing hyperparameter tuning during the model's training phase. Despite these areas for enhancement, this study highlights the potential of using metaheuristic optimization algorithms to optimize the architecture of network models effectively.

ACKNOWLEDGMENT

The authors would like to express their appreciation to the Biomaterials and Tissue Engineering Laboratory (BiMaTEL) and the Intelligent Systems Laboratory (ISL) of De La Salle University, Manila, for their valuable help.

REFERENCES

[1] E. Darwin and M. Tomic-Canic, "Healing chronic wounds: Current challenges and potential solutions," *Current Dermatology Rep.*, vol. 7, no. 4, pp. 296–302, Dec. 2018, doi: 10.1007/s13671-018-0239-4.

[2] J. C. J. Holzer-Geissler, S. Schwingenschuh, M. Zacharias, J. Einsiedler, S. Kainz, P. Reisenegger, C. Holecek, E. Hofmann, B. Wolff-Winiski, H. Fahrngruber, T. Birngruber, L.-P. Kamolz, and P. Kotzbeck, "The impact of prolonged inflammation on wound healing," *Biomedicines*, vol. 10, no. 4, p. 856, Apr. 2022, doi: 10.3390/biomedicines10040856.

[3] S. Li, P. Renick, J. Senkowsky, A. Nair, and L. Tang, "Diagnostics for wound infections," *Adv. Wound Care*, vol. 10, no. 6, pp. 317–327, Jun. 2021, doi: 10.1089/wound.2019.1103.

[4] M. Haalboom, M. H. E. Blokhuis-Arkes, R. J. Beuk, R. Meerwaldt, R. Klont, M. J. Schijffelen, P. B. Bowler, M. Burnet, E. Sigl, and J. A. M. van der Palen, "Culture results from wound biopsy versus wound swab: Does it matter for the assessment of wound infection?" *Clin. Microbiology Infection*, vol. 25, no. 5, pp. 629e7–629e12, May 2019, doi: 10.1016/j.cmi.2018.08.012.

[5] E. M. Jones, C. A. Cochrane, and S. L. Percival, "The effect of pH on the extracellular matrix and biofilms," *Adv. Wound Care*, vol. 4, no. 7, pp. 431–439, Jul. 2015, doi: 10.1089/wound.2014.0538.

[6] D. Kim, R. S. Concepcion, G. A. M. Espiritu, J. R. H. S. Agueda, and R. R. P. Vicerra, "Optimized fuzzy logic and adaptive neuro-fuzzy inference systems for wound healing time prediction among the diabetic patients," in *Proc. 8th Int. Conf. Bus. Ind. Res. (ICBIR)*, Bangkok, Thailand, May 2023, pp. 536–542.

[7] A. Abdollahi, H. Roghani-Mamaqani, and B. Razavi, "Stimuli-chromism of photoswitches in smart polymers: Recent advances and applications as chemosensors," *Prog. Polym. Sci.*, vol. 98, Nov. 2019, Art. no. 101149, doi: 10.1016/j.progpolymsci.2019.101149.

[8] V. Březina, S. Ishihara, J. Lang, L. Hanyková, K. Ariga, J. P. Hill, and J. Labuta, "Structural modulation of chromic response: Effects of binding-site blocking in a conjugated calix[4]pyrrole chromophore," *Chem. Open*, vol. 7, no. 5, pp. 323–335, May 2018, doi: 10.1002/open.201800005.

[9] D. K. Nguyen, Q.-V. Bach, J.-H. Lee, and I.-T. Kim, "Synthesis and irreversible thermochromic sensor applications of manganese violet," *Materials*, vol. 11, no. 9, p. 1693, Sep. 2018, doi: 10.3390/ma11091693.

[10] R. Toivola, S.-H. Jang, S. Baker, A. K.-Y. Jen, and B. D. Flinn, "Thermochromic polymer film sensors for detection of incipient thermal damage in carbon fiber–epoxy composites," *Sensors*, vol. 18, no. 5, p. 1362, Apr. 2018, doi: 10.3390/s18051362.

[11] K. Devarayan, P. Pandiyan, K. S. Nagaraju, and H. Anjappan, "Halochromic sensors for real-time monitoring of spoilage of packed seer fish," *Mater. Today, Proc.*, vol. 33, pp. 3961–3966, Jul. 2020, doi: 10.1016/j.matpr.2020.06.332.

[12] A. Noshirvani Sharifabad and S. H. Bahrami, "Halochromic chemosensor from poly(acrylonitrile)/phenolphthalein nanofibers as pH sensor," *IEEE Sensors J.*, vol. 16, no. 4, pp. 873–880, Feb. 2016, doi: 10.1109/JSEN.2015.2495338.

[13] N. Ha, K. Xu, G. Ren, A. Mitchell, and J. Z. Ou, "Machine learning-enabled smart sensor systems," *Adv. Intell. Syst.*, vol. 2, no. 9, Sep. 2020, Art. no. 2000063, doi: 10.1002/aisy.202000063.

[14] H. Yao, X. Zhang, X. Zhou, and S. Liu, "Parallel structure deep neural network using CNN and RNN with an attention mechanism for breast cancer histology image classification," *Cancers*, vol. 11, no. 12, p. 1901, Nov. 2019, doi: 10.3390/cancers11121901.

[15] H. Liu, S. Wang, G. Jing, Z. Yu, J. Yang, Y. Zhang, and Y. Guo, "Combined CNN and RNN neural networks for GPR detection of railway subgrade diseases," *Sensors*, vol. 23, no. 12, p. 5383, Jun. 2023, doi: 10.3390/s23125383.

[16] S. Sun, Z. Cao, H. Zhu, and J. Zhao, "A survey of optimization methods from a machine learning perspective," *IEEE Trans. Cybern.*, vol. 50, no. 8, pp. 3668–3681, Aug. 2020, doi: 10.1109/TCYB.2019.2950779.
[17] M. Sarhani, S. Voß, and R. Jovanovic, "Initialization of metaheuristics: Comprehensive review, critical analysis, and research directions," *Int. Trans. Oper. Res.*, vol. 30, no. 6, pp. 3361–3397, Nov. 2023, doi: 10.1111/itor.13237.
[18] A. G. Janairo, J. J. Baun, R. Concepcion, R.-J. Relano, K. Francisco, M. L. Enriquez, A. Bandala, R. R. Vicerra, M. Alipio, and E. P. Dadios, "MeterFTX: Shuffled frog leap-optimized feed forward neural network applied on transmitter monitoring system for multi-array antenna subsurface imaging," in *Proc. 8th Int. Conf. Bus. Ind. Res. (ICBIR)*, Bangkok, Thailand, May 2023, pp. 662–668.
[19] M. A. Cohen, T. L. Botch, and C. E. Robertson, "The limits of color awareness during active, real-world vision," *Proc. Nat. Acad. Sci. USA*, vol. 117, no. 24, pp. 13821–13827, Jun. 2020, doi: 10.1073/pnas.1922294117.
[20] X.-S. Yang, "Nature-inspired optimization algorithms: Challenges and open problems," *J. Comput. Sci.*, vol. 46, Oct. 2020, Art. no. 101104, doi: 10.1016/j.jocs.2020.101104.
[21] A.-N. Sharkawy, "Principle of neural network and its main types: Review," *J. Adv. Appl. Comput. Math.*, vol. 7, pp. 8–19, Aug. 2020, doi: 10.15377/2409-5761.2020.07.2.
[22] C. Maldonado, F. Mora-Poblete, R. I. Contreras-Soto, S. Ahmar, J.-T. Chen, A. T. do Amaral, and C. A. Scapim, "Genome-wide prediction of complex traits in two outcrossing plant species through deep learning and Bayesian regularized neural network," *Frontiers Plant Sci.*, vol. 11, Nov. 2020, Art. no. 593897, doi: 10.3389/fpls.2020.593897.
[23] K. López-Aguilar, A. Benavides-Mendoza, S. González-Morales, A. Juárez-Maldonado, P. Chiñas-Sánchez, and A. Morelos-Moreno, "Artificial neural network modeling of greenhouse tomato yield and aerial dry matter," *Agriculture*, vol. 10, no. 4, p. 97, Apr. 2020, doi: 10.3390/agriculture10040097.
[24] H. A. Shehadeh, "Chernobyl disaster optimizer (CDO): A novel metaheuristic method for global optimization," *Neural Comput. Appl.*, vol. 35, no. 15, pp. 10733–10749, May 2023, doi: 10.1007/s00521-023-08261-1.
[25] S. Talatahari and M. Azizi, "Chaos game optimization: A novel metaheuristic algorithm," *Artif. Intell. Rev.*, vol. 54, no. 2, pp. 917–1004, Feb. 2021, doi: 10.1007/s10462-020-09867-w.
[26] M. A. Al-Betar, Z. A. A. Alyasseri, M. A. Awadallah, and I. Abu Doush, "Coronavirus herd immunity optimizer (CHIO)," *Neural Comput. Appl.*, vol. 33, no. 10, pp. 5011–5042, May 2021, doi: 10.1007/s00521-020-05296-6.
[27] D. Giavarina, "Understanding bland Altman analysis," *Biochemia Medica*, vol. 25, no. 2, pp. 141–151, Jun. 2015, doi: 10.11613/bm.2015.015.
[28] S. Karamizadeh, S. M. Abdullah, A. A. Manaf, M. Zamani, and A. Hooman, "An overview of principal component analysis," *J. Signal Inf. Process.*, vol. 4, pp. 173–175, Aug. 2013.
[29] N. M. Rezk, M. Purnaprajna, T. Nordström, and Z. Ul-Abdin, "Recurrent neural networks: An embedded computing perspective," *IEEE Access*, vol. 8, pp. 57967–57996, 2020, doi: 10.1109/ACCESS.2020.2982416.
[30] M. Z. Arshad, A. Jamsrandorj, J. Kim, and K. Mun, "Gait events prediction using hybrid CNN-RNN-based deep learning models through a single waist-worn wearable sensor," *Sensors*, vol. 22, no. 21, p. 8226, Oct. 2022.
[31] S. E. Zieger and K. Koren, "Machine learning for optical chemical multianalyte imaging," *Anal. Bioanal. Chem.*, vol. 415, no. 14, pp. 2749–2761, Apr. 2023, doi: 10.1007/s00216-023-04678-8.
[32] D. Li and L. Li, "Detection of water pH using visible near-infrared spectroscopy and one-dimensional convolutional neural network," *Sensors*, vol. 22, no. 15, p. 5809, Aug. 2022, doi: 10.3390/s22155809.

DAEUK KIM was born in Bucheon, South Korea, in 1997. He is currently pursuing the B.S. and M.S. degrees in manufacturing engineering with De La Salle University.

His research interests include smart wound management, wearable sensors, polymer science, and the application of artificial intelligence in the biomedical engineering field.

RONNIE S. CONCEPCION, II (Member, IEEE) was born in Philippines, in 1991. He received the B.S. degree in electronics and communications engineering from the Technological University of the Philippines, Manila, Philippines, the M.S. degree in electronics engineering with a specialization in microelectronics from Mapua University, Manila, and the Ph.D. degree in electronics and communications engineering with a specialization in applied artificial intelligence in biosystems from De La Salle University (DLSU), Manila.

He is currently an Associate Professor and the Advanced Studies Coordinator of the Department of Manufacturing Engineering and Management, DLSU, and a Visiting Scientist with the Center for Plant Molecular Biology, Universität Tübingen, Germany. His research interests include evolutionary computing, cellular physiology, digital phenomics, polymer science, and the application of artificial intelligence in biosystems and biomedical engineering.

Dr. Concepcion, II's awards and honors include the Outstanding Young Scientist 2023 of the Philippines National Academy of Science and Technology, the 2023 Outstanding ASEAN Science Diplomat, the Green Talents 2022 Award granted by German Federal Ministry of Education and Research in Berlin, Germany, and the Top 2% of the World's Scientists in 2022 based on composite citation indicators of Stanford University.

JOSEPH REY H. STA. AGUEDA received the B.S. and M.S. degrees in manufacturing engineering from De La Salle University (DLSU), where he is currently pursuing the Ph.D. degree in chemical engineering.

He is currently an Assistant Professor with the Department of Manufacturing and Management, DLSU, and the Project Leader of Biomaterials and Tissue Engineering Laboratories (BiMaTEL), DLSU. He recently did extensive training in polymer studies and 3-D bioprinting with Case Western Reserve University, Cleveland, OH, USA, under DOST Sponsorship. He is also involved on research work funded internally by DLSU and with grants from CHED under their DARETO grant, DOST PCIEERD for training and research, and also in partnerships with institutions like the National Kidney Transplant Institute (NKTI). His current research interests include biomaterials development, tissue engineering, regenerative medicine, and additive manufacturing.

JOHN MARTIN S. MONDRAGON received the M.S. degree in biology from De La Salle University, supported by the DOST-ASTHRDP Scholarship. His master's thesis centered on the formulation of an extracellular matrix (ECM)-based hydrogel derived from pig kidney tissue. He has been a Research Specialist with Biomaterials and Tissue Engineering Laboratories (BiMaTEL), De La Salle University, since 2018. He is currently interested in pursuing further education and research in biomaterial development, biomedical engineering, and tissue engineering, reflecting a keen focus on advancing knowledge at the intersection of biology and materials.